


Dissipative Self-Assembly Hot Paper
How to cite: *Angew. Chem. Int. Ed.* **2024**, *63*, e202409169

doi.org/10.1002/anie.202409169

Non-Equilibrium Dissipative Assembly with Switchable Biological Functions

Peng Zhao⁺, Yuanfeng Zhao⁺, Yan Lu, Linjie Xu, Bohan Li, Yingshuai Zhao, Wei Zhou, Pu Yan, Youfu Wang, Kecheng Cao, and Yijun Zheng*

Abstract: Natural dissipative assembly (DSA) often exhibit energy-driven shifts in natural functions. However, creating man-made DSA that can mimic such biological activities transformation remains relatively rare. Herein, we introduce a cytomembrane-like dissipative assembly system based on chiral supramolecules. This system employs benzoyl cysteine in an out of equilibrium manner, enabling the shifts in biofunctions while minimizing material use. Specifically, aroyl-cystine derivatives primarily assemble into stable M-helix nanofibers under equilibrium conditions. These nanofibers enhance fibroblast adhesion and proliferation through stereospecific interactions with chiral cellular membranes. Upon the addition of chemical fuels, these functional nanofibers temporarily transform into non-equilibrium nanospheres, facilitating efficient drug delivery. Subsequently, these nanospheres revert to their original nanofiber state, effectively recycling the drug. The programmable function-shifting ability of this DSA establishes it as a novel, fuel-driven drug delivery vehicle. And the bioactive DSA not only addresses a gap in synthetic DSAs within biological applications but also sets the stage for innovative designs of 'living' materials.

Introduction

Dissipative self-assembly (DSA) in living organisms facilitated most biological processes like cellular motility, signal transduction and self-replication.^[1] The energy-fueled non-equilibrium supramolecular assemblies undergo an energetically downhill pathway to equilibrium state, dominating the temporal operation of physiological activity.^[2] Great achievements in material science have been made to mimic

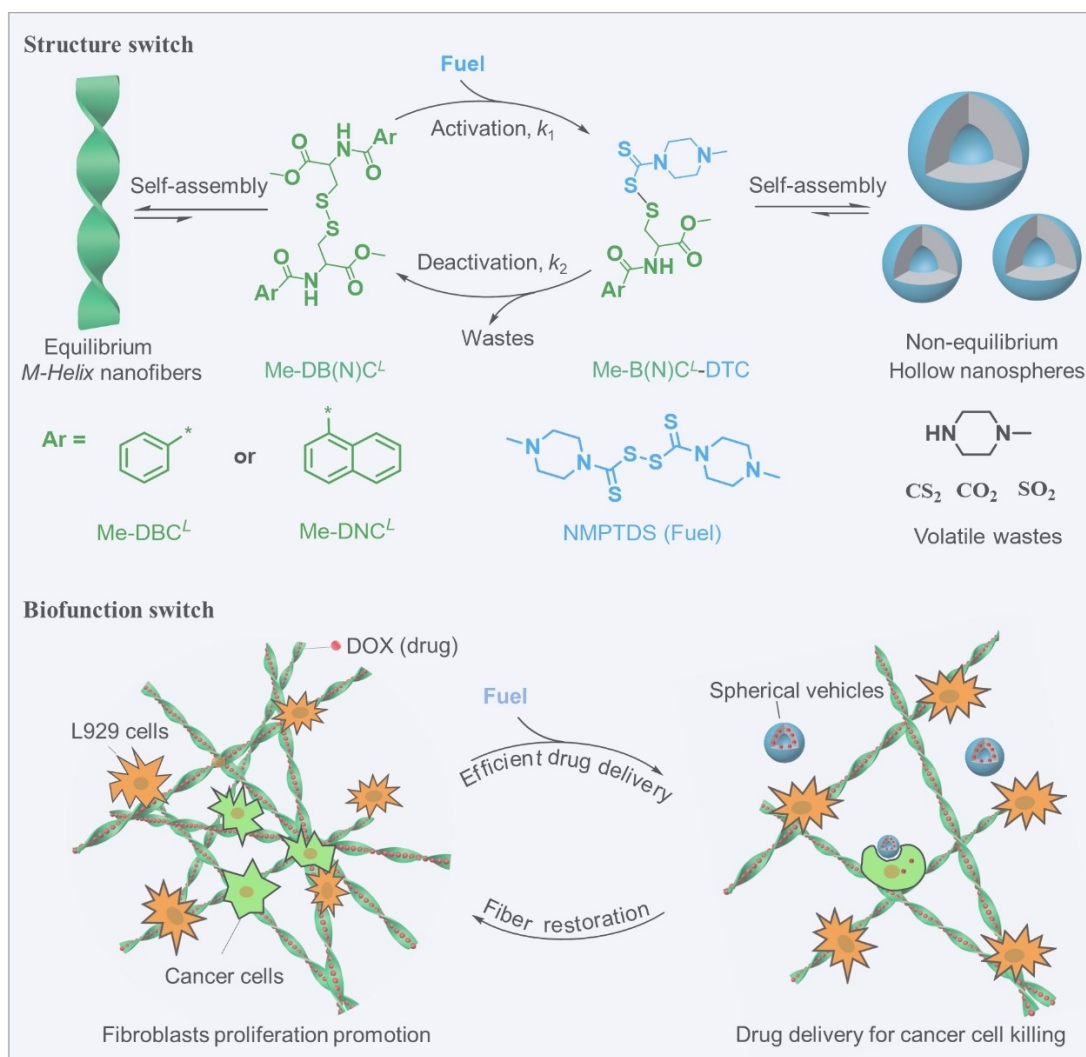
the DSA process, often starting from soluble precursors and transforming them into non-equilibrium assemblies, including transient fibers,^[3] vesicles,^[4] micelles^[5] and metal clusters.^[6] However, these synthetic assemblies still don't match the complex bioactivity of their natural counterparts.^[7] The discrepancy arises partly because, in living systems, the equilibrium precursors are not only primed for transition into functional DSA but also engage in additional biological activities. This allows for a diverse integration of functions at minimal material costs. For instance, the cell membrane, dynamically constructed through the self-assembly of chiral phospholipids, provides structural integrity to the cell,^[8] within which the chirality of phospholipids is essential for cellular processes such as signaling, recognition, and interaction.^[9] Additionally, upon stimulation by high-energy molecules like guanosine triphosphate (GTP), this dynamic lipid membrane can transform into intraluminal vesicles for proteins/mRNA transport to recipient cells.^[10] Following delivery, the phospholipids blocks of exosomes can reuse into the cell membrane to maintain its integrity or prepare for the next transport cycle, a process driven by the hydrolysis of GTP.^[10b,c,11] This cycle exemplifies a DSA process in which phospholipids are efficiently reused for different biofunctions, and highlighting the complexity and efficiency of cellular operations.^[12] Achieving such sophisticated biofunction shifting using minimal materials by synthetic DSA systems would help take a further step towards artificial "living" materials but this remains a significant hurdle.^[13]

To this end, herein, we present a membrane-like DSA system endowed with swiftable biological functions, including chiral scaffolds for fibroblasts proliferation promotion or advanced drug delivery for cancer cell killing. The system utilizes chiral aroyl-cystine derivatives, specifically Me-DB-(N)C^L, which naturally form equilibrium nanofibers exhibiting supramolecular chirality (Scheme 1). Subsequently, N-methylpiperazino-thiuram disulfides (NMPTDS), acting as a fuel, initiate a disulfide-disulfide metathesis reaction to form Me-DB(N)C^L-DTC conjugates. This reaction triggers a structural transition from the fibrous assembly to non-equilibrium hollow nanospheres. As the fuel depletes, these out-of-equilibrium structures revert to nanofibers, constituting a DSA process. The nanofibers as functional assemblies instead of non-assembling precursors enabled an additional biofunctional integration in complex DSA and biological functions from the equilibrium state could be maintained even without fuels, a basis for developing DSAs with switchable biological functions like cell membrane. Our

[*] P. Zhao,⁺ Y. Zhao,⁺ Y. Lu, L. Xu, B. Li, Y. Zhao, W. Zhou, P. Yan, K. Cao, Y. Zheng
School of Physical Science and Technology & State Key Laboratory of Advanced Medical Materials and Devices, ShanghaiTech University, 201210 Shanghai, China
E-mail: zhengyj@shanghaitech.edu.cn

Y. Wang
School of Chemistry and Chemical Engineering, Shanghai Jiao Tong University, 200240 Shanghai, China

[†] These authors contributed equally.



Scheme 1. Dissipative self-assembly (DSA) system with shifting structure and biological functions, based on biocompatible disulfides. The aryl L-cysteine derivatives, Me-DB(N) C^L , initially form the chiral nanofibers to promote fibroblast adhesion/proliferation. These chiral nanofibers also serve as hydrophobic drugs reservoir, such as doxorubicin (DOX). The introduction of N-methylpiperazino-thiuram disulfide (NMPTDS) as fuel initiates a disulfide-disulfide metathesis reaction with Me-DB(N) C^L , transforming the nanofibers into non-equilibrium hollow nanospheres (activation phase), thereby enhancing the rate of drug release for cancer cell eradication. As the fuel depletes, the out-of-equilibrium Me-DB(N) C^L -DTC assemblies revert to the chiral nanofibers, encapsulating DOX again (deactivation phase).

findings highlight the scientific significance of this system in several ways. Firstly, the equilibrium nanofibers serving as chiral hydrogel scaffolds promoted fibroblast cell adhesion and proliferation—a process significantly influenced by supramolecular chirality. Secondly, the nanofibers as a drug reservoir could be transitioned into the non-equilibrium nanospherical carriers for targeted cancer cell eradication upon the addition of chemical fuel. Most notably, our system allows the recovery of excess drugs into equilibrium nanofibers after achieving therapeutic objectives, providing a novel fuel-driven drug delivery vehicle.

Results and Discussion

Design and Synthesis of DSA based on Disulfides

The design of the dissipative self-assembling system presented here begins with methylated dibenzoyl-L-cysteine (Me-DBC L), a well-documented hydrogelator that relies on disulfide bond.^[3a,14] When Me-DBC L is dissolved in a dimethyl sulfoxide/H₂O mixture (20 mM, 5:95) at pH 7.2, it forms nanofibers (Video S1) due to the presence of periodic hydrogen bonds and hydrophobic interactions.^[15] The entangled fibrillar network is responsible to the formation of physical hydrogels (Figure 1a) with a storage modulus of 1500 Pa (G' , Figure 1b). Intriguingly, 12 hours after the addition of N-methylpiperazino-thiuram disulfide (NMPTDS, a biocompatible disulfiram derivative^[16]), the

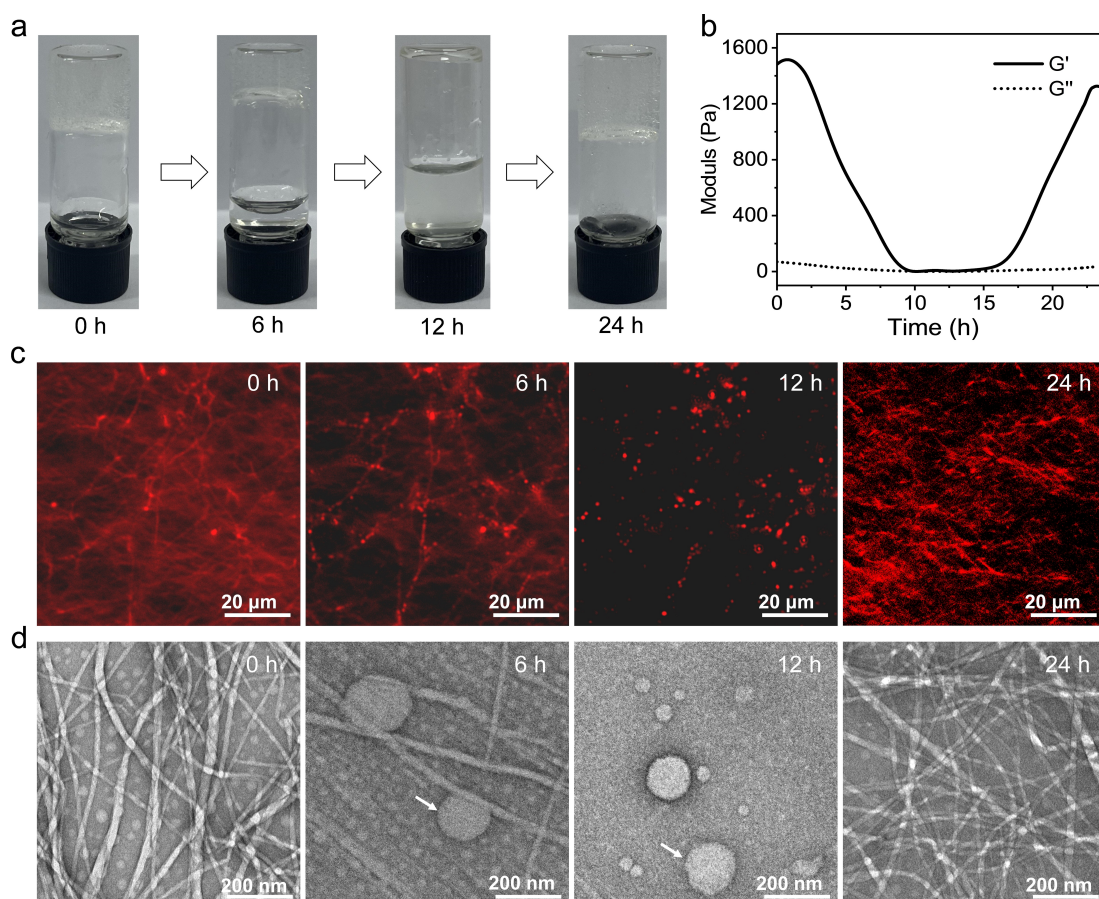


Figure 1. (a) Time-dependent gel-solution-gel transition of Me-DBC^L hydrogels in DMSO/H₂O (5:95) at pH 7.2, induced by adding NMPTDS fuel. (b) Rheology characterization of the dissipative assembly formed by Me-DBC^L and NMPTDS; (c&d) CLSM and TEM images showing the evolution of the dissipative assembly. Initial Me-DBC^L nanofibers decrease due to disulfide-disulfide metathesis (indicated by white arrows showing non-equilibrium Me-BC^L-DTC assemblies), followed by an increase as Me-BC^L-DTC undergoes a decomposition reaction (deactivation). For confocal microscopy, Nile red was used to label the assembly structures, with an excitation wavelength of 528 nm. The initial concentrations of [Me-DBC^L]₀, NMPTDS and Nile red were optimized to 10 mM, 12 mM and 3 μmol, respectively. For TEM analysis, the samples were stained with uranyl acetate.

hydrogels undergo a transition into a colloidal solution (Figure S1), significantly reducing the G' to 11 Pa (Figure 1a&1b). Subsequently, the colloidal solution reverts to hydrogel form within 24 h, suggesting a reversible microstructure transition, entirely spontaneously.

To track the changes in assembly, confocal laser scanning microscopy (CLSM) was utilized with hydrophobic Nile red as a fluorescence marker. Initially, Me-DBC^L and Nile Red were dissolved in dimethyl sulfoxide, followed by the addition of 95 vol % H₂O to initiate assembly. The initial concentration of [Me-DBC^L]₀ was optimized to 10 mM to achieve a suitable fiber density and timeframe for capturing the microscopic assemblies dynamically. As shown in Figure 1c& Video S1, 12 hours post NMPTDS addition, most fibers were replaced by spherical assemblies. By the 24 hours mark, these spherical assemblies had transitioned back to fibers. We also used transmission electron microscopy (TEM, Figure 1d) to confirm this evolution process and we found the nanofibers with an average width of 10 nm shifted to out-of-equilibrium nanospheres with a diameter of 200 nm. This characteristic morphological transformation

from nanofibers to nanospheres could be ascribed to the disulfide-disulfide exchange reaction between Me-DBC^L and NMPTDS (activation, Scheme 1 & Figure S2). The resulting out-of-equilibrium assembly, comprising Me-BC^L-DTC, is inherently unstable and gradually reverts to Me-DBC^L nanofiber (deactivation process).^[17] The activation/deactivation process with a reaction rate constant of 0.014 M⁻¹s⁻¹ and 0.0014 M⁻¹s⁻¹ in chemical reaction network, forms a dissipative cycle. This could be further verified by replacing Me-DBC^L with methylated dinaphthaloyl-L-cystine (Me-DNC^L) or D-cystines (Me-DBC^D), as demonstrated in Figure S3 & S4.

Structural Characteristics and Interaction Mechanisms of the Non-Equilibrium Assembly

To obtain detailed insights into the non-equilibrium spherical structure, scanning transmission electron microscope (STEM) and energy dispersive spectrometer (EDS) were employed. The corona distribution of C, N and O elements

in the mapping analysis (Figure 2a) indicated a hollow structure (wall thickness ~ 42 nm).^[18] The hollow characteristics was further supported by z-axis-dependent CLSM images and the observation of globular fusion (Figure S5). Drawing parallels with Me-DBC^L nanofibers, where hydrogen bonding and amphiphilic interactions drive supramolecular assembly,^[15] we proposed that the amide hydrogen bonds also contribute to the stability of the non-equilibrium Me-BC^L-DTC assembly. This hypothesis was explored using hydrogen nuclear magnetic resonance (¹H NMR, Figure 2b), where the successive addition of D₂O to the Me-BC^L-DTC solution caused shifts in the chemical shifts of amide and aromatic hydrogen towards lower and higher magnetic fields, respectively. This shift is attributed to the enhanced NH–CO intermolecular interactions and shielding effect from aryl π – π stacking (see below).^[19] The presence of amide hydrogen bonds in Me-BC^L-DTC was confirmed by Fourier-transform infrared spectroscopy (FTIR, Figure 2c). For the amorphous powder of Me-BC^L-DTC, the peaks at 3330 and 1637 cm⁻¹, attributed to ν N–H

and ν C=O vibration of amide groups, bathochromically shifts to 3327 and 1635 cm⁻¹ in a freeze-dried sample of the nanospherical assembly, mirroring the NH–CO interactions.^[19] Powder X-ray diffraction (PXRD) analysis (Figure 2d) revealed a crystalline nature of the non-equilibrium assembly,^[20] echoing the characteristics of Me-BC^L-DTC needle-like single crystals formed by slow evaporation (more details, please see Figure S6 and Table S1). This crystallinity facilitated the investigation of intermolecular interactions within the Me-BC^L-DTC assembly, revealing a possible network formed by N–H \cdots O=C bonds, planar π – π stacking, and amphiphilic interactions as shown in Figure 2e. Four Me-BC^L-DTC molecules constitute a stacking module with a distance of 3.5 nm (dashed polygons). And with additional considerations for the aqueous extension of the inner/outer protonated Me-BC^L-DTC molecules (positively charged), the 42 nm wall thickness suggests a twelvefold repetition of the stacking module. The thickness was found to vary with pH, decreasing in acidic conditions (Figure S7), which aligns with the protonation behavior of Me-BC^L-DTC

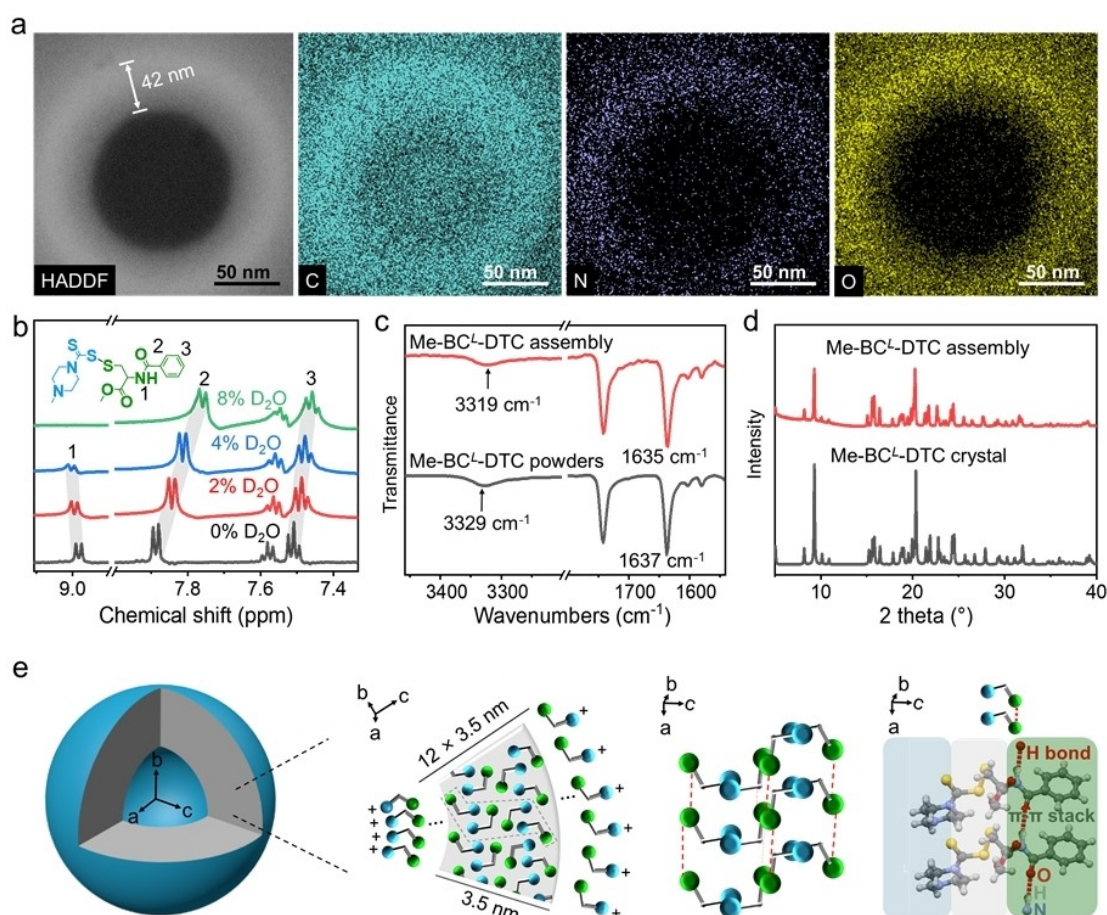


Figure 2. (a) Scanning transmission electron microscopy (STEM) with high-angle annular dark field detector (HAADF) and energy dispersive X-ray spectroscopy (EDS) element mapping analysis across a single non-equilibrium Me-BC^L-DTC nanosphere, collected from the Me-DBC^L fueled with NMPTDS in CH₂OH/H₂O (5:95) at 12 h; (b) Proton nuclear magnetic resonance (¹H NMR) spectra showing hydrogen bond interactions with varying amount of deuterium water (D₂O) in DMSO-d₆; (c) Infrared spectra comparing amorphous Me-BC^L-DTC and the freeze-dried assembly; (d) Powder X-ray diffraction (PXRD) spectra comparison between the single crystal and the freeze-dried assembly of Me-BC^L-DTC; (e) An envisaged model to illustrate the stacking and arrangement of Me-BC^L-DTC within the non-equilibrium hollow nanospheres. Blue and green balls represent the hydrophilic methyl piperazine and hydrophobic benzoyl domains respectively. Grey sticker represent disulfide centers.

and its reduced hydrophobic encapsulation at lower pH levels ($pK_a=8.3$).^[21]

Tunable Lifetime and Cycle Stability Evaluation

Controlling the kinetics of the dissipative process is of critical importance to allow subsequent life activities to occur before reaching equilibrium.^[22] To this end, we then explored the time-scale regulation of the non-equilibrium assembly and discovered that the lifetime of the non-equilibrium nanospheres increases as the pH decreases (Figure 3a). For instance, assemblies at pH 8 exhibited a duration of ~4 hours, while those formed at pH 5 displayed significantly extended lifetime of approximately 12 hours. This extension is likely due to the declined deactivation rate of Me-BC^L-DTC at lower pH levels, considering the base-catalyzed deactivation reaction.^[23] Moreover, elevating the NMPTDS/Me-DBC^L ratio also led to a prolonged transient lifetime (Figure 3b), likely by effectively inhibiting the deactivation reaction (Figure S8). We observed that the nitrogen flow rate significantly impacts the lifespan, reducing it from 6 hours at 0 L/min to 3 hours at 6 L/min (Figure 3c). This phenomenon is attributed to the rapid removal of volatile byproducts by hydrolysis (N-methylpiperazine, CS₂, SO₂ and CO₂), accelerating the deactivation reaction.^[24] The design of the precursors also influences the dissipative process. For instance, non-equilibrium assemblies created using Me-DNC^L displayed shorter lifetime compared to those made with Me-DBC^L (Figure 3d). Benefiting from the naphthalene group with superior hydrophobicity and π - π stacking ability,^[25] Me-DNC^L is more

stable than Me-DBC^L and the self-assembling nanofibers decreased the concentration of Me-DNC^L in solutions, promoting the deactivation reaction (Me-NC^L-DTC hydrolysis). The cycle stability of the dissipative system was examined using high performance liquid chromatography (HPLC) and dynamic light scattering (DLS) analysis. As shown in Figure 3e&f, even after 3 cycles, the Me-DBC^L concentration and its hydrodynamic diameter were largely restored, with only a negligible decline observed. The slight decrease in the concentration of Me-DBC^L and Me-BC^L-DTC after each cycle (Figure 3e), is probably due to the formation of polysulfide byproducts (Figure S9), in which the increased molecular flexibility of polysulfides diminishes the crystallization efficiency.^[26]

Chirality Control of the Equilibrium Assembly for Fibroblast Cell Adhesion/Proliferation Promotion

Chiral supramolecular hydrogels have attracted considerable research interest due to their resemblance to the native extracellular matrix (ECM) and their potential as a versatile toolkit for modulating cellular behavior.^[27] Given that Me-DBC^L features two chiral centers, it's anticipated that the equilibrium fibers resulting from its self-assembly will manifest chirality. To investigate the chiral properties of these assemblies, circular dichroism (CD) were firstly employed. Me-DBC^L in CH₃OH displayed a weak CD signal at 219 and 236 nm, a reflection of its molecular chirality. Intriguingly, a pronounced positive ($\lambda_{max}=216$ nm) signal and a subtle negative (241 nm) CD signal were observed when adding H₂O into the Me-DBC^L solution (Figure 4a),

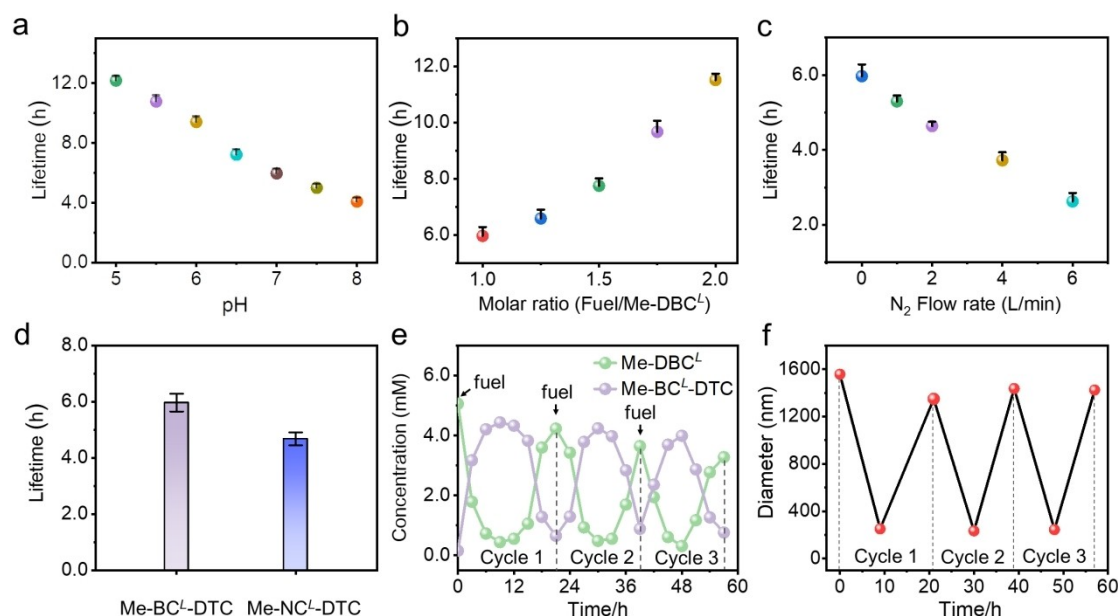


Figure 3. (a) pH-dependent lifetime of the non-equilibrium nanospheres; The lifetime influenced by the fuels/Me-DBC^L molar ratio (b), nitrogen flow rate (c) and the precursors (d); (e&f) Cycle stability of the dissipative system evaluated using high performance liquid chromatography (HPLC) and dynamic light scattering (DLS) analysis. The transient lifetime was assessed using the inverted tube test ($n=3$) and the initial concentrations for [Me-DBC^L]₀ and NMPTDS were set as 10 mM and 12 mM (pH 7.2).

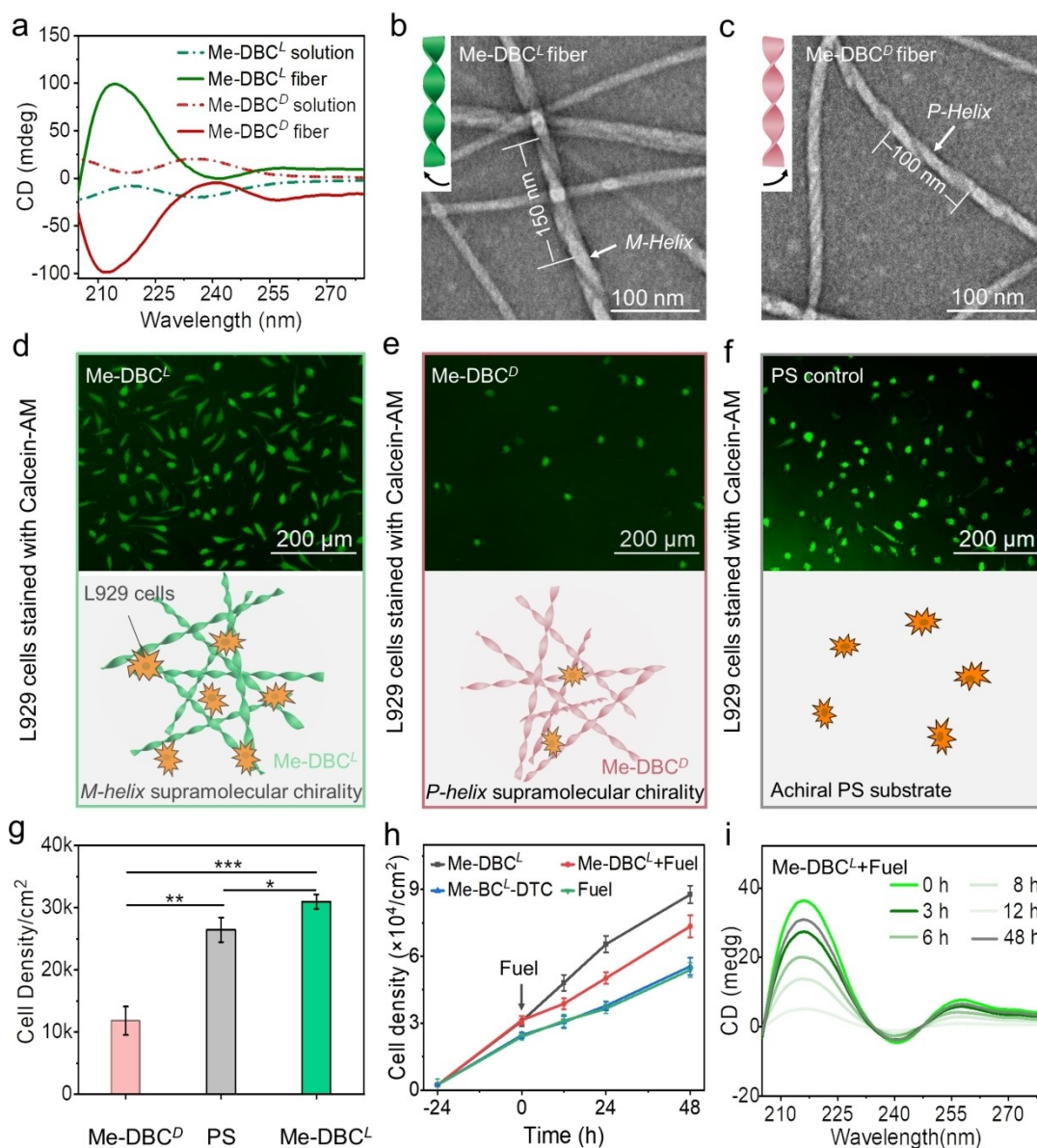


Figure 4. (a) CD signal of Me-DBC^D and Me-DBC^L in CH₃OH or CH₃OH/H₂O; (b & c) TEM images of left-handed helical (*M*-helix) nanofibers in the Me-DBC^L xerogel and right-handed helical (*P*-helix) nanofibers of Me-DBC^D; (d) L929 cells cultured for 24 hours on the PS substrate coated with Me-DBC^L xerogel and a schematic illustration of L929 cell adhesion/proliferation on the substrates, all the cells were stained with Calcein-AM; (e) L929 cells on the PS substrate coated with Me-DBC^D xerogel; (f) The cells on the PS substrate; (g) L929 cell density statistics from several fluorescence microscope images ($n=5$), the cells were cultured on different substrate for 24 hours; (h) Time-dependent L929 cells density ($n=3$), after co-cultured for 24 hours, the fuel was only added at 0 h for Fuel and Me-DBC^L + Fuel groups. 2 eq fuel was added to Me-BC^L-DTC group to maintain the stability in culture medium; (i) CD spectra change of Me-DBC^L + Fuel system.

indicating the formation of single-handed supramolecular helix due to the asymmetric assembly of Me-DBC^L.^[28] These findings were corroborated by detailed TEM and cryo-TEM (Figure 4b & Figure S10), which revealed left-handed twisted nanofibers with a helical pitch of around 75 nm (*M*-helix). We also explored the influence of the enantiomers on supramolecular helix. The supramolecular assemblies of *D*-cystine derivatives (Me-DBC^D) exhibited a right-handed twisted nanofiber with a helical pitch of 50 nm (*P*-helix, Figure 4c). This helicity inversion was in good correlation with the CD spectra of the hydrogels.

To further assess the effect of these chiral assemblies on cell adhesion/proliferation, mouse fibroblast cells (L929) were cultured on the substrate coated with Me-DBC^L or Me-DBC^D nanofibers, using a polystyrene (PS) well as a control. After co-culture for 24 h, cells on Me-DBC^L exhibited enhanced spreading morphologies, as evidenced by Calcein-AM staining (Figure 4d). In contrast, cell adhesion was found to be inhibited on the *P*-helix Me-DBC^D compared to the PS control group (Figure 4e & 4f). Quantitative analysis in Figure 4g revealed that Me-DBC^L supported the highest cell density ($3.1 \times 10^5/\text{cm}^2$), which was 1.2

and 2.6 times greater than those observed on PS and Me-DBC^D surfaces, respectively. To further confirm the role of supramolecular chirality, we evaluate the cell density from Me-BC^L-DTC (without supramolecular chirality), Me-DBC^L and Me-DBC^L+Fuel (Figure 4h). Compared to the Me-BC^L-DTC, the Me-DBC^L group showed a higher cell density (Figure 4h). And upon adding the fuel, the Me-DBC^L+Fuel group showed a reduced cell density than Me-DBC^L at 12 h, due to the dissolution of supramolecular chirality (Figure 4i). Interestingly, an accelerated proliferation in Me-DBC^L+Fuel group was observed at 48 h upon rebuilding the supramolecular chirality. The aforementioned results indicated the *M-helix* supramolecular chirality from Me-DBC^L probably benefit the stereospecific interaction with chiral cell membrane and increase cell adhesion/proliferation by cooperative effect.^[29] Moreover, the ability to transiently deactivate this promotive effect by introducing fuel offers a possibility for biological function switch akin to those observed in cell membranes.^[30]

Fuel-Driven Drug Delivery: Utilizing Non-Equilibrium Nanospheres for Customized Cancer Therapy

Hydrogel-based local drug delivery systems represent an innovative treatment approach that can be administered intraoperatively to directly release encapsulated therapeutic agents at unresectable tumor sites. This method offers significant advantages over systemic chemotherapy, including a reducing systemic toxicity and sustained release of high-concentration drugs at tumor site for efficient tumor inhibition. In these systems, responsive hydrogels were desired to achieve effective biological distribution and controlled release of drugs.^[31] Inspired by this, we proposed the concept of fuel-driven drug release using non-equilibrium nanospheres, which allowed for the creation of predictable, non-linear drug release profiles contingent on the amount of fuel added. As an illustrative example, the hydrophobic chemotherapy agent doxorubicin (DOX) was encapsulated within the Me-DBC^L nanofibers at a loading efficiency of 5 wt % and the *in vitro* drug release kinetics was assessed by UV/Vis absorption spectroscopy (more details, please see Supporting Information).^[32] Three experimental groups plus with one control group were selected, including Me-DBC^L+Fuel^{a+b} and Me-DBC^L alone ('a' and 'b' indicate fuel added at 0 and 22 h, respectively, at an equivalent ratio relative to Me-DBC^L). As shown in Figure 5a, the release kinetics of DOX could be modulated by varying the fuel dosage and the timing of fuel additions. For instance, the Me-DBC^L group exhibited a slow drug release profile, with less than 5 % DOX released by 12 h. The introduction of fuel resulted in 80 % and 39 % of the DOX being released within the same timeframe in Me-DBC^L+Fuel¹⁺¹ and Me-DBC^L+Fuel^{0.5+0} group. This rapid drug release is attributable to the transformation of the nanofibers into non-equilibrium nanospheres. And the positively-charged non-equilibrium nanospheres with smaller size (Figure 2e) are preferentially taken up by cancer cells.^[29]

To reveal this better, the nanofiber loaded with DOX were coated on the polystyrene (PS) substrate for co-culture with representative cervical cancer cells (Hela) as model cell lines. And the density of residual Hela cells was counted from several CLSM images (Figure S11). As shown in Figure 5b, the Me-DBC^L+Fuel¹⁺¹ group showed a declined Hela cell density as early as 12 h after fuel addition, accompanied by a transition in cellular morphology from spread to round shapes (Figure 5c). In stark contrast, the DOX-encapsulated nanofibers (Me-DBC^L group) exhibited red fluorescence upon excited with a 480 nm laser and most of Hela cells survived at 36 hours post-incubation. By 36 hours, the majority of Hela cells in Me-DBC^L+Fuel¹⁺¹ was killed, with a cell density of 1500/cm², which is only 20 % of that in the Me-DBC^L groups. In contrast, the Me-DBC^L+Fuel^{0.5+0} group demonstrated a cell density of 4900 cells/cm² at 36 hours (Figure 5b & Figure S12), which is 1.7 and 3.4 times greater than the Me-DBC^L+Fuel^{0.5+0.5} and Me-DBC^L+Fuel¹⁺¹ groups, respectively. And no obvious cell viability decline caused by the wastes was observed (Figure S13). These results indicated that the fuel-driven drug release using non-equilibrium nanospheres allowed for the creation of predictable, non-linear drug release profiles for customized cancer cell killing. To obtain more details on the drug delivery, the DOX in non-equilibrium nanospheres (red fluorescence signal) and LysoTracker Green DND-26 (green fluorescence signal) were co-localized by CLSM. The results indicated that the red fluorescence of DOX was mainly distributed in the cytoplasm at 2 h (Figure 5d). And by extending the co-culture time to 4 h, a significant separation between the red and green fluorescence was observed, indicating the onset of efficient lysosomal escape, despite some remaining yellow fluorescence indicative of partial co-localization. By the 12 h mark, the presence of a more intense red fluorescence within the cytoplasm, distinct from the LysoTracker (green), suggested the successful release of most DOX into the cytoplasm.^[33] Concurrently, a reduced green fluorescence from the LysoTracker (Figure 5e) indicated the protonation of the internal Me-BC^L-DTC structures (Figure 2e),^[34] which likely raised the pH within the lysosomal compartment, disrupting the lysosomes through a proton sponge effect.^[35] This disruption enabled the drugs to escape the lysosome and penetrate the nucleus, where they efficiently inhibit DNA and RNA synthesis by blocking replication and transcription processes and cause the cancer cells death (Figure 5f).^[36]

To this extent, we have developed a membrane-like DSA system, that achieves complex biofunction integration through the switchable use of benzoyl cysteine, akin to phospholipids in biological membranes, enabled by a chemical fuel (Scheme 1). Firstly, the equilibrium chiral scaffolds, with/without DOX, could promote fibroblasts proliferation (Figure S14). When fueled by NMPTDS, these scaffolds, also serving as drug reservoirs, temporarily transform into non-equilibrium nanospheres for efficient drug delivery. As the fuel depletes, the out-of-equilibrium nanospherical assemblies revert to nanofibers, recycling DOX (Figure 5a & c). This constitutes a chemical fuel-driven switch between fibroblasts proliferation promotion and

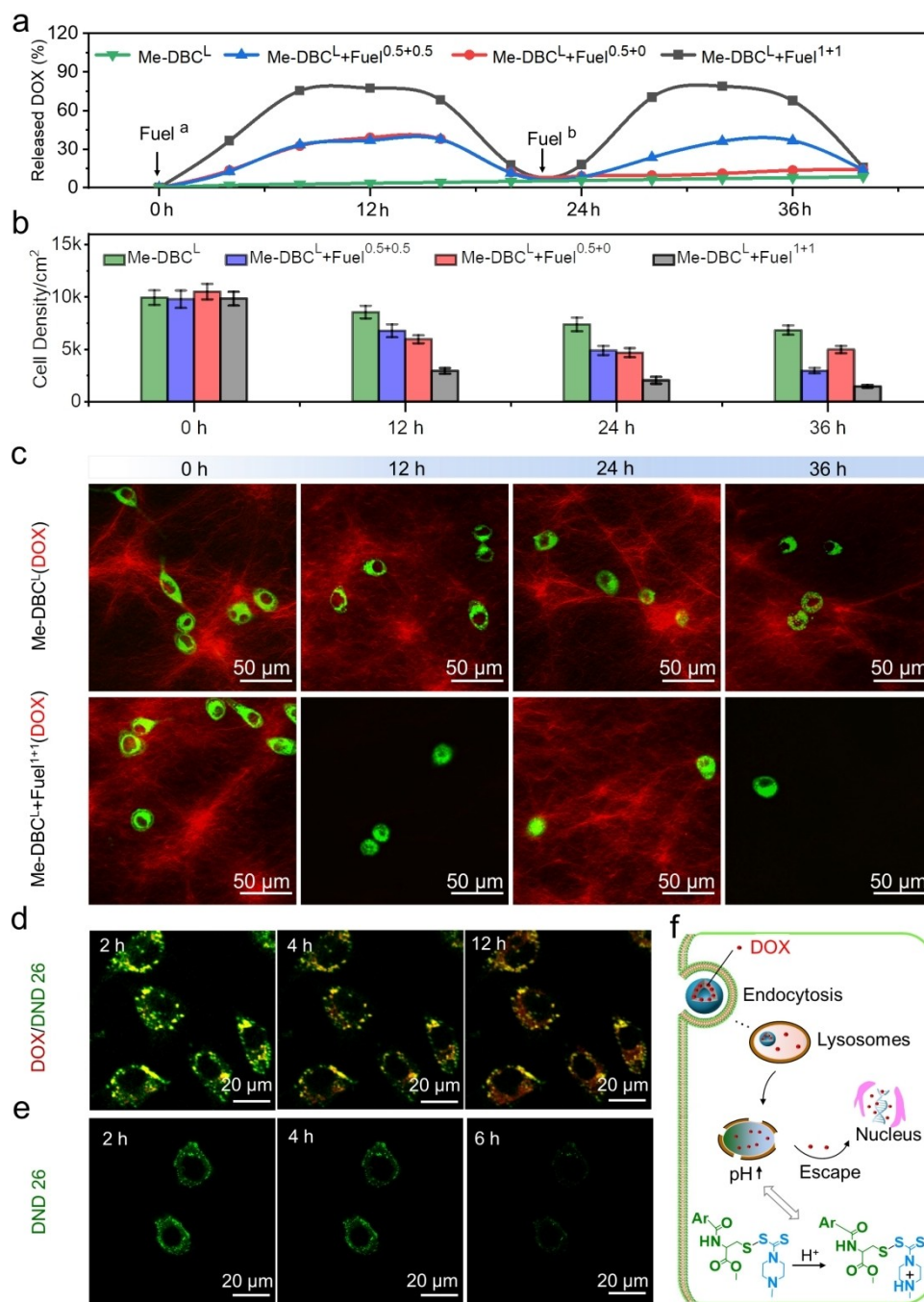


Figure 5. (a) Release kinetics of DOX in the nanofibers determined by UV/Vis adsorption. Three experimental groups and one control group were selected, including the Me-, PS Me-DBC^L+Fuel^{a+b} and DBC^L group ($n=3$). 'a' and 'b' respectively represented the added fuel at 0 and 22 h, equivalent ratio relative to Me-DBC^L. (b) Time-dependent density of residual HeLa cells on different substrate, counted from Figure S11. (c) CLSM of the HeLa cells on Me-DBC^L substrate. The assembly encapsulated with DOX were visualized by using 488 nm laser and the emission wavelength at 575–585 nm were collected (red fluorescence signal). The HeLa cells were regenerated according the pseudo-color images from bright field photos. (d) CLSM images of HeLa cells co-localized with LysoTracker Green DND-26 (green fluorescence signal) and the DOX (red fluorescence signal) in non-equilibrium nanospheres. (e) Time-dependent CLSM images of the HeLa cells stained with LysoTracker Green DND-26. (f) The proposed drug delivery pathway from the fueled non-equilibrium nanospheres.

efficient drug delivery. Utilizing biocompatible chiral aroyl-cystine derivatives, we unlock the potential of synthetic DSAs in biology.^[37] The fuel-switchable activities in DSAs also elucidate how complex biofunctions can be integrated

with minimal materials costs, advancing the development of artificial “living” materials.

Conclusions

In summary, we developed a dissipative assembly system based on chiral supramolecules, utilizing benzoyl cysteine in a switchable manner for sophisticated biofunction shifts at minimal material cost. This includes applications as chiral scaffolds and drug reservoirs, as well as for efficient drug delivery. We demonstrated that the equilibrium M-helix supramolecular chirality enhances fibroblast cell adhesion and proliferation through the cooperative effects of molecular and supramolecular chirality. Upon the addition of chemical fuels, the functional nanofibers serving as drug reservoirs were temporarily converted into non-equilibrium nanospheres, which then effectively recycled the drug back into equilibrium nanofibers, constituting a novel chemical fuel-driven drug delivery vehicle. We found that the positively charged non-equilibrium nanospheres could efficiently deliver drugs by electrostatic bonding with cell membranes and escape from lysosomes. The reported DSA with biological activities unlock the potential of man-made DSA in biology. Especially, the switchable bioactivities enable a complex function integration using minimal materials, which would initiate a fashion for ingenious design of “living” materials.

Supporting Information

Supporting Information is available from the Wiley Online Library or from the author.

Acknowledgments

This work was supported by the National Natural Science Foundation of China (52073175 and 22107064), National Natural Science Foundation of Shanghai (23ZR1442700), and ShanghaiTech University. We thank the support from the Analytical Instrumentation Center (contract no. SPST-AIC10112914), SPST, ShanghaiTech University. We also thank Xinqiu Guo and Jing Liu in the Instrumental Analysis Center of SJTU for cryo-TEM analysis.

[CCDC 2349485 contains the supplementary crystallographic data for this paper. These data can be obtained free of charge from The Cambridge Crystallographic Data Centre via www.ccdc.cam.ac.uk/data_request/cif.]

Conflict of Interest

The authors declare no conflict of interest.

Data Availability Statement

The data that support the findings of this study are available from the corresponding author upon reasonable request.

Keywords: Dissipative self-assembly · out of equilibrium systems · chiral supramolecules · fuel-driven drug delivery · nanofiber-nanosphere transition

- [1] a) S. De, R. Klajn, *Adv. Mater.* **2018**, *30*, 1706750; b) K. Das, L. Gabrielli, L. J. Prins, *Angew. Chem. Int. Ed.* **2021**, *60*, 20120–20143.
- [2] G. Ragazzon, L. J. Prins, *Nat. Nanotechnol.* **2018**, *13*, 882–889.
- [3] a) J. Boekhoven, W. E. Hendriksen, G. J. M. Koper, R. Eelkema, J. H. van Esch, *Science* **2015**, *349*, 1075–1079; b) F. Klepel, B. J. Ravoo, *Org. Biomol. Chem.* **2017**, *15*, 3840–3842; c) S. A. P. van Rossum, M. Tena-Solsona, J. H. van Esch, R. Eelkema, J. Boekhoven, *Chem. Soc. Rev.* **2017**, *46*, 5519–5535; d) J. S. Valera, A. López-Acosta, T. M. Hermans, *Angew. Chem. Int. Ed.* **2024**, e202406931; e) T. M. Hermans, N. Singh, *Angew. Chem. Int. Ed.* **2023**, *62*, e202301529; f) M. D. Pol, K. Dai, R. Thomann, S. Moser, S. K. Roy, C. G. Pappas, *Angew. Chem. Int. Ed.* **2024**, *136*, e202404360.
- [4] a) S. Maiti, I. Fortunati, C. Ferrante, P. Scrimin, L. J. Prins, *Nat. Chem.* **2016**, *8*, 725–731; b) G. Wang, Y. Liu, Y. Liu, N. Xia, W. Zhou, Q. Gao, S. Liu, *Colloids Surf. A* **2017**, *529*, 808–814; c) K. Das, H. Kar, R. Chen, I. Fortunati, C. Ferrante, P. Scrimin, L. Gabrielli, L. J. Prins, *J. Am. Chem. Soc.* **2023**, *145*, 898–904; d) Z. H. Zhang, M. G. Howlett, E. Silvester, P. Kukura, S. P. Fletcher, *J. Am. Chem. Soc.* **2024**, *146*, 18262–18269.
- [5] a) B. G. P. van Ravensteijn, I. K. Voets, W. K. Kegel, R. Eelkema, *Langmuir* **2020**, *36*, 10639–10656; b) C. Pan, J. Xu, L. Wang, Y. Jia, J. Li, G. Liu, S. Zhu, B. Yang, Y. Li, *CCS Chem.* **2023**, *5*, 669–681; c) X. Lang, Y. Huang, L. He, Y. Wang, U. Thumu, Z. Chu, W. T. S. Huck, H. Zhao, *Nat. Commun.* **2023**, *14*, 3084; d) S. M. Morrow, I. Colomer, S. P. Fletcher, *Nat. Commun.* **2019**, *10*, 1011.
- [6] a) P. Zhao, L. Xu, B. Li, Y. Zhao, Y. Zhao, Y. Lu, M. Cao, G. Li, T.-C. Weng, H. Wang, Y. Zheng, *Adv. Mater.* **2024**, *36*, 2311818; b) H. Lee, J. Tessarolo, D. Langbehn, A. Baksi, R. Herges, G. H. Clever, *J. Am. Chem. Soc.* **2022**, *144*, 3099–3105; c) S. Hollstein, M. von Delius, *Acc. Chem. Res.* **2024**, *57*, 602–612.
- [7] a) H. Wang, Y. Song, W. Wang, N. Chen, B. Hu, X. Liu, Z. Zhang, Z. Yu, *J. Am. Chem. Soc.* **2024**, *146*, 330–341; b) A. Sorrenti, J. Leira-Iglesias, A. J. Markvoort, T. F. A. de Greef, T. M. Hermans, *Chem. Soc. Rev.* **2017**, *46*, 5476–5490; c) N. Singh, G. J. M. Formon, S. De Piccoli, T. M. Hermans, *Adv. Mater.* **2020**, *32*, 1906834.
- [8] a) Y. C. Lin, C. Chipot, S. Scheuring, *Nat. Commun.* **2020**, *11*, 230; b) A. Angelova, B. Angelov, M. Drechsler, T. Bizien, Y. E. Gorshkova, Y. R. Deng, *Front. Cell. Dev. Biol.* **2021**, *9*, 617984; c) E. H. Mojumdar, C. Grey, E. Sparr, *Int. J. Mol. Sci.* **2020**, *21*, 56; d) L. P. Liu, Y. K. Zou, A. Bhattacharya, D. Y. Zhang, S. S. Q. Lang, K. N. Houk, N. K. Devaraj, *Nat. Chem.* **2020**, *12*, 1029.
- [9] a) B. Chang, M. Zhang, G. Qing, T. Sun, *Small* **2015**, *11*, 1097–1112; b) M. Zhang, G. Qing, T. Sun, *Chem. Soc. Rev.* **2012**, *41*, 1972–1984.
- [10] a) A. Desai, T. J. Mitchison, *Annu. Rev. Cell Dev. Biol.* **1997**, *13*, 83–117; b) M. Jurasek, M. Cernohorska, J. Rehulka, V. Spiwok, T. Sulimenko, E. Draberova, M. Darmostuk, S. Gurska, I. Frydrych, R. Burianova, T. Ruml, M. Hajduch, P. Bartunek, P. Draber, P. Dzubak, P. B. Drasar, D. Sedlak, *J. Steroid Biochem.* **2018**, *183*, 68–79; c) D. Melgari, C. Barbier, G. Dilanian, C. Rucker-Martin, N. Doisne, A. Coulombe, S. N. Hatem, E. Balse, *J. Mol. Cell. Cardiol.* **2020**, *144*, 127–139.
- [11] a) R. de Rooij, E. Kuhl, *Biophys. J.* **2018**, *114*, 201–212; b) K. Dai, M. D. Pol, L. Saile, A. Sharma, B. Liu, R. Thomann, J. L. Trefs, D. Y. Qiu, S. Moser, S. Wiesler, B. N. Balzer, T. Hugel,

- H. J. Jessen, C. G. Pappas, *J. Am. Chem. Soc.* **2023**, *145*, 26086–26094.
- [12] a) J. T. Kindt, J. W. Szostak, A. N. Wang, *ACS Nano* **2020**, *14*, 14627–14634; b) R. Fernandez-Garcia, J. C. Munoz-Garcia, M. Wallace, L. Fabian, E. Gonzalez-Burgos, M. P. Gomez-Serranillos, R. Raposo, F. Bolas-Fernandez, M. P. Ballesteros, A. M. Healy, Y. Z. Khimiyak, D. R. Serrano, *J. Controlled Release* **2022**, *341*, 716–732; c) A. Englert, F. Majer, J. L. Schiessl, A. J. C. Kuehne, M. von Delius, *Chem* **2024**, *10*, 910–923.
- [13] a) O. E. Shklyayev, A. C. Balazs, *Nat. Nanotechnol.* **2024**, *19*, 146–159; b) M. Sun, J. Deng, A. Walther, *Angew. Chem. Int. Ed.* **2023**, *62*, e202214499; c) K. Liu, A. Blokhuis, C. van Ewijk, A. Kiani, J. Wu, W. H. Roos, S. Otto, *Nat. Chem.* **2024**, *16*, 79–88.
- [14] J. Boekhoven, A. M. Brizard, K. N. K. Kowlgi, G. J. M. Koper, R. Eelkema, J. H. van Esch, *Angew. Chem. Int. Ed.* **2010**, *49*, 4825–4828.
- [15] F. M. Menger, K. L. Caran, *J. Am. Chem. Soc.* **2000**, *122*, 11679–11691.
- [16] Y.-x. Xu, Y.-y. Huang, R.-r. Song, Y.-l. Ren, X. Chen, C. Zhang, F. Mao, X.-k. Li, J. Zhu, S.-s. Ni, J. Wan, J. Li, *Eur. J. Med. Chem.* **2020**, *203*, 112500.
- [17] Y. Zhao, P. Zhao, J. Zhang, Y. Zhao, B. Li, G. Hao, Y. An, W. Zhou, Y. Lu, L.-Y. Chou, Y. Zheng, *CCS Chem.* **2023**, *6*, 1571–1580.
- [18] a) S. Liu, C. Dun, Q. Jiang, Z. Xuan, F. Yang, J. Guo, J. J. Urban, M. T. Swihart, *Nat. Commun.* **2024**, *15*, 1167; b) P. Zhao, J. Zhang, A. Mohsin, J. Huang, X. Hou, X. Jin, X. Zhu, *Appl. Surf. Sci.* **2022**, *596*, 153589.
- [19] a) Y. J. Li, X. Ran, Q. Y. Li, Q. Q. Gao, L. J. Guo, *Chem. Asian J.* **2016**, *11*, 2157–2166; b) Q. Zhang, S. Crespi, R. Toyoda, R. Costil, W. R. Browne, D.-H. Qu, H. Tian, B. L. Feringa, *J. Am. Chem. Soc.* **2022**, *144*, 4376–4382; c) H. Feng, N. Zheng, W. Peng, C. Ni, H. Song, Q. Zhao, T. Xie, *Nat. Commun.* **2022**, *13*, 397.
- [20] S. Kandambeth, V. Venkatesh, D. B. Shinde, S. Kumari, A. Halder, S. Verma, R. Banerjee, *Nat. Commun.* **2015**, *6*, 6786.
- [21] a) P. Zhao, L. Wang, Y. Wu, T. Yang, Y. Ding, H. G. Yang, A. Hu, *Macromolecules* **2019**, *52*, 4376–4384; b) Y. Hao, J. Wang, J. Ma, X. Yu, Z. Li, S. Wu, S. Tian, H. Ma, S. He, X. Zhang, *Bioorg. Chem.* **2023**, *137*, 106584.
- [22] E. Roduner, S. G. Radhakrishnan, *Chem. Soc. Rev.* **2016**, *45*, 2768–2784.
- [23] J. Zhang, J. Liu, H. Li, X. Li, Y. Zhao, P. Zhao, J. Cui, B. Yang, Y. Song, Y. Zheng, *ACS Appl. Mater. Interfaces* **2022**, *14*, 20073–20082.
- [24] J. Tang, Y. Cheng, M. Ding, C. Wang, *ChemPlusChem* **2023**, *88*, e202300449.
- [25] a) R. K. Cheedarala, J.-H. Jeon, C.-D. Kee, I.-K. Oh, *Adv. Funct. Mater.* **2014**, *24*, 6005–6015; b) P. Zhao, Y. Dai, Y. Wu, L. Wang, B. Huang, Y. Ding, A. Hu, *Polym. Chem.* **2017**, *8*, 5734–5740.
- [26] R. A. Pérez-Camargo, R. d'Arcy, A. Iturrospe, A. Arbe, N. Tirelli, A. J. Müller, *Macromolecules* **2019**, *52*, 2093–2104.
- [27] a) X. Wang, B. Wu, Y. Zhang, X. Dou, C. Zhao, C. Feng, *Acta Biomater.* **2022**, *153*, 204–215; b) J. Li, Y. Cui, Y.-L. Lu, Y. Zhang, K. Zhang, C. Gu, K. Wang, Y. Liang, C.-S. Liu, *Nat. Commun.* **2023**, *14*, 5030; c) J. L. Greenfield, J. Wade, J. R. Brandt, X. Shi, T. J. Penfold, M. J. Fuchter, *Chem. Sci.* **2021**, *12*, 8589–8602.
- [28] G. Liu, X. Li, J. Sheng, P.-Z. Li, W. K. Ong, S. Z. F. Phua, H. Ågren, L. Zhu, Y. Zhao, *ACS Nano* **2017**, *11*, 11880–11889.
- [29] a) J. Liu, F. Yuan, X. Ma, D.-i. Y. Auphedeous, C. Zhao, C. Liu, C. Shen, C. Feng, *Angew. Chem. Int. Ed.* **2018**, *57*, 6475–6479; b) H. Lu, Y. Zhao, S. Qin, Y. Zhang, J. Liu, J. Zhang, C. Feng, W. Zhao, *Adv. Fiber Mater.* **2023**, *5*, 377–387.
- [30] a) L. Albert, O. Vázquez, *Chem. Commun.* **2019**, *55*, 10192–10213; b) L. Wang, Y. Xue, J. Xing, K. Song, J. Lin, *Annu. Rev. Plant Biol.* **2018**, *69*, 525–551.
- [31] a) Z. Sun, C. Song, C. Wang, Y. Hu, J. Wu, *Mol. Pharmaceutics* **2020**, *17*, 373–391; b) Y. Shao, L. Xiang, W. Zhang, Y. Chen, *J. Controll. Release* **2022**, *352*, 600–618; c) J. Li, D. J. Mooney, *Nat. Rev. Mater.* **2016**, *1*, 16071; d) F. Rizzo, N. S. Kehr, *Adv. Healthcare Mater.* **2021**, *10*, 2001341; e) M. Lei, Q. Wang, R. Gu, D.-H. Qu, *Responsive Materials* **2024**, *2*, e20230027.
- [32] D.-H. Kim, D. C. Martin, *Biomaterials* **2006**, *27*, 3031–3037.
- [33] a) Y. Wang, Y.-X. Lin, Z.-Y. Qiao, H.-W. An, S.-L. Qiao, L. Wang, R. P. Y. J. Rajapaksha, H. Wang, *Adv. Mater.* **2015**, *27*, 2627–2634; b) A. Paillard, F. Hindré, C. Vignes-Colombeix, J.-P. Benoit, E. Garcion, *Biomaterials* **2010**, *31*, 7542–7554.
- [34] D. Schmaljohann, *Adv. Drug Delivery Rev.* **2006**, *58*, 1655–1670.
- [35] J. Aguiar, P. Carpena, J. A. Molina-Bolívar, C. Carnero Ruiz, *J. Colloid Interface Sci.* **2003**, *258*, 116–122.
- [36] M. Norouzi, V. Yathindranath, J. A. Thliveris, B. M. Kopec, T. J. Sahaan, D. W. Miller, *Sci. Rep-UK* **2020**, *10*, 11292.
- [37] R. K. Grötsch, A. Angi, Y. G. Mideksa, C. Wanzke, M. Tena-Solsona, M. J. Feige, B. Rieger, J. Boekhoven, *Angew. Chem. Int. Ed.* **2018**, *57*, 14608–14612.

Manuscript received: May 15, 2024

Accepted manuscript online: August 22, 2024

Version of record online: October 17, 2024